Fabrication of 3D flower-like black N-TiO$_{2-x}$@MoS$_2$ for unprecedented-high visible-light-driven photocatalytic performance

Xuefeng Liu[a], Zipeng Xing[a,*], Yan Zhang[a], Zhenzi Li[b], Xiaoyan Wu[b], Siyu Tan[a], Xiujuan Yu[a], Qi Zhu[a], Wei Zhou[a,*]

[a] Department of Environmental Science, School of Chemistry and Materials Science, Key Laboratory of Functional Inorganic Material Chemistry, Ministry of Education of the People's Republic of China, Heilongjiang University, Harbin, 150080, PR China
[b] Department of Epidemiology and Biostatistics, Harbin Medical University, Harbin, 150086, PR China

ARTICLE INFO

ABSTRACT

As is well-known, it is a great challenge that the smooth TiO$_2$ nanospheres are coated by MoS$_2$ nanosheets to form the core-shell nanostructure owing to their poor interaction. Herein, we report 3D black N-TiO$_{2-x}$@MoS$_2$ core-shell nanostructures synthesized by a mild and effective strategy combined with a typical hydrothermal reaction and an in situ solid-state chemical reduction method followed by 350 °C calcination under an argon atmosphere. The prepared samples are characterized in detail by X-ray diffraction, Raman, scanning electron microscopy, transmission electron microscopy, and X-ray photoelectron spectroscopy. The results suggest that the 3D N-TiO$_{2-x}$@MoS$_2$ photocatalyst is successfully doped with N and Ti^{3+}, and simultaneously coupling with MoS$_2$ to form the core-shell heterojunction nanostructure. The N and Ti^{3+} co-doped and hybrid heterostructures can effectively utilize visible-light and solar energy to degrade methyl orange and produce hydrogen. The degradation rate of methyl orange and the hydrogen production rate are as high as 91.8% and 1.882 mmol h^{-1} g^{-1}. To the best of our knowledge, this work is the first instance of combining MoS$_2$ with N and Ti^{3+} co-doped TiO$_2$, and the proposed photocatalytic mechanism will provide a new perspective for high activity photocatalyst in future.

© 2016 Elsevier B.V. All rights reserved.

1. Introduction

Semiconductor photocatalysis for eliminating environmental pollutants and splitting water to produce hydrogen by utilizing solar energy has been recognized as one of the most efficient strategies to solve the environment and energy crisis [1]. TiO$_2$, as one of promising semiconductor photocatalysts, has been widely investigated for pollutant degradation [2,3], dye-sensitized solar cells [4–6], photoelectrochemical electrodes [7,8] and other photocatalytic applications [9,10] because of its nontoxicity, high physical and chemical stability, and strong oxidizability. [11–13] Unfortunately, there are two major barriers that have hampered industrial-scale application of pure TiO$_2$ in the photocatalytic process. The one is its wide band gap (3.2 eV for anatase), which restricts its photocatalytic activity under visible light. The other is the rapid recombination of photogenerated electron-hole pairs,

which results in the low efficiency of photoinduced chemical reactions [14,15]. Therefore, proposing reasonable approaches to narrow the band gap and restrain the recombination of photogenerated electron-hole pairs for high-efficient photocatalysts is essential.

To our knowledge, the photocatalytic performance of TiO$_2$ can be enhanced by two major strategies including impurity element doping and forming a semiconductor heterojunction. Firstly, impurity element doping in TiO$_2$ is an intelligent strategy through introducing sub-bandgap states or narrowing the band gap in order to broaden the absorption from UV to visible light region [16,17]. Secondly, forming a semiconductor heterojunction by coupling TiO$_2$ with a secondary substance contributes to inhibit the photogenerated electron-hole pairs recombination and accelerate the transfer of electrons [18–20]. Then, if these two strategies can be simultaneously adopted by a modified TiO$_2$ photocatalyst, the photocatalytic performance will be obviously enhanced. Therefore, designing TiO$_2$ combined with impurity doping and coupling with other semiconductor materials has become a hotspot based on the synergistic application efficiency [21,22].

Among the metal or nonmetal doping, N doping and Ti^{3+} self-doping have been attracted considerable interest owing to the significant effect for improving photocatalytic activity [23,24]. Doping TiO_2 with nitrogen contributes to narrow band gap through embedding nitrogen atom into the lattice of TiO_2, which can create the overlap of oxygen 2p states and nitrogen 2p states on the top of the valence band (VB) of TiO_2 at substitutional lattice sites, thus enhancing the response of photocatalytic activity in visible light region [25]. Ti^{3+} self-doping TiO_2 achieves the same purpose due to the local states will be formed at the bottom of the conduction band (CB) of TiO_2 by introducing Ti^{3+} or oxygen vacancies (Ov) into the lattice [26]. Despite the interest in the effects of nitrogen doping and Ti^{3+} self-doping, there are only a few reports about the N and Ti^{3+} co-doping on the photocatalytic activity of TiO_2. Son et al. has reported a method to synthesize the N and Ti^{3+} co-doping TiO_2 by cotreatment with H_2 and NH_3 under high temperature (500 °C), which results in the enhancement in the water oxidation performance under visible light illumination [27]. However, the high temperature, hydrogenation and direct amination synthesis routes are not safe and less suitable for practical application. Therefore, a mild and appropriate method should be designed and developed to synthesize the N and Ti^{3+} co-doping TiO_2.

Among the inorganic materials, MoS_2 as a typical layered transition metal sulfide with a structure composed of three stacked atom layers (S-Mo-S) has been a focus of research for long time because of narrow band gap [28], wonderful morphologies [29] and extensive application including lithium batteries [30], hydrogen production [31] and photocatalysis.[32]. To date, various morphologies MoS_2 are always used to combine with other semiconductors to form a 3D semiconductor heterojunction structure to increase more active sites than 1D and 2D nanostructured materials owing to the active S atoms on the exposed edges of MoS_2 and decrease electron-hole pairs recombination [33,34]. In particular, the MoS_2/TiO_2 is one of the best composite photocatalysts, which shows excellent photocatalytic performance compared with pure TiO_2 [35]. Nevertheless, the photocatalytic performance of the MoS_2/TiO_2 composite photocatalyst in the visible-light region is not satisfactory for practical applications. Therefore, this kind of system should be further developed to enhance the utilization efficiency of solar energy.

Herein, in this paper, we present a mild and effective synthetic method for preparing the N and Ti^{3+} co-doping TiO_2, and simultaneously coupling with MoS_2 to form semiconductor heterojunction core-shell structure. To the best of our knowledge, no prior work is reported about this kind of TiO_2. In addition, the visible photocatalytic activity of the as-prepared sample has been proved by removing methyl orange and splitting water to produce hydrogen, and a possible mechanism is also proposed which the N and Ti^{3+} co-doping and introduction of MoS_2 synergistically lead to improving visible photocatalytic activity due to reduce band gap and restrain the recombination of photogenerated electron-hole pairs. We believe that the preparation method provides a green, mild and effective way for the rational design of $N-TiO_{2-x}@MoS_2$.

2. Materials and synthesis

2.1. Materials

Tetrabutyl titanate (TBOT), absolute ethanol (EtOH), urea and concentrated hydrochloric acid (HCl) were purchased from Tianjin Kermel Chemical Reagent Co. Ltd, China. Molybdenum trioxide (MoO_3), potassium rhodanate (KSCN) and sodium boron hydride ($NaBH_4$, 98%) were purchased from Aladdin Reagent Company, China. All the chemicals used in this study were analytical grade and employed without further purification.

2.2. Synthesis

2.2.1. Preparation of the $N-TiO_2$ nanospheres

The 0.4 g of urea, as the nitrogen source, was dissolved in 50 mL of absolute ethanol with 10 min of magnetic stirring. While still stirring, 2 mL of hydrochloric acid (HCl) and 8 mL of tetrabutyl titanate (TBOT) were slowly added, respectively. After magnetic stirring for 2 h, the mixture was transferred into a 100 mL Teflon-lined stainless steel autoclave, which was heated at 150 °C for 4 h. The obtained yellowish powders were washed with deionized water three times to remove any ionic residue, and then centrifuged and dried at 80 °C for 12 h. The as-prepared sample was denoted as $N-TiO_2$. For comparsion, the pure TiO_2 was also synthesized under the same condition without adding urea.

#### 2.2.2. Preparation of 3D black $N-TiO_{2-x}@MoS_2$ core-shell structures

0.2 g of molybdenum trioxide (MoO_3) and 0.5 g of potassium rhodanate (KSCN) were dissolved in 30 mL deionized water to form a mixed solution with 0.5 h of magnetic stirring. Then 1.0 g of the obtained $N-TiO_2$ was put into the mixed solution. After magnetic stirring for 1 h, the mixed solution was transferred to a 50 mL Teflon-lined stainless steel autoclave which was heated at 200 °C for 18 h. The obtained composite sample was washed with deionized water and absolute ethanol, centrifuged and dried at 80 °C for 12 h. Subsequently, the 0.8 g of composite sample was ground with 0.8 g of $NaBH_4$ at room temperature (20 ±2 °C) for 30 min thoroughly. Then the mixtures were transferred into porcelain boats, and placed in a tubular furnace to calcine at 350 °C for 2 h under the Ar atmosphere [36]. After naturally cooling down to room temperature, the black $N-TiO_{2-x}@MoS_2$ was obtained (Scheme 1) and washed with deionized water three times to remove unreacted $NaBH_4$. For comparsion, the MoS_2 and $N-TiO_2@MoS_2$ were also synthesized under the same condition in the absence of $N-TiO_2$, and $NaBH_4$, respectively.

2.3. Characterization

X-ray diffraction (XRD) was carried out on a Bruker D 8 Advance diffractometer by using Cu Kα radiation source (α = 0.15418 nm). The morphologies of these samples were examined by using a field emission scanning electron microscope (FE-SEM, Hitachi S-4800). Transmission electron microscope (TEM) JEOL JEM-2010 at an accelerating voltage of 200 kV was also used to record the electron micrographs of the samples. X-ray photoelectron spectroscopy (XPS) was carried out on a Kratos- ULTRA AXIS DLD with Al Kα X-ray source. All binding energies were calibrated with surface adventitious carbon of 284.6 eV. The UV–vis diffuse reflectance spectra (DRS) were performed on a TU-1901 spectrophotometer using $BaSO_4$ as the background over a range of 190–800 nm. The •OH radicals were detected by the fluorescence probe technique with terephthalic acid (FL-TA) on a RF-5301PC fluorescence spectrophotometer.

2.4. Photoelectrochemical measurement

Photoelectrochemical measurements were recorded using an electrochemical workstation (CHI760E, Shanghai) with a standard three-electrode system. To prepare the photoelectrode, 50 mg of photocatalyst sample was mixed with 35 mL of terpineol under the condition of stirring. The suspension was dip-coated onto the 2 cm² FTO-glass electrode and then heated at 200 °C for 2 h in Ar. The as-prepared photoelectrode, Pt sheet and Ag/AgCl were used as the working electrode, counter electrode and reference electrode, respectively. All photoelectrochemical measurements were con-
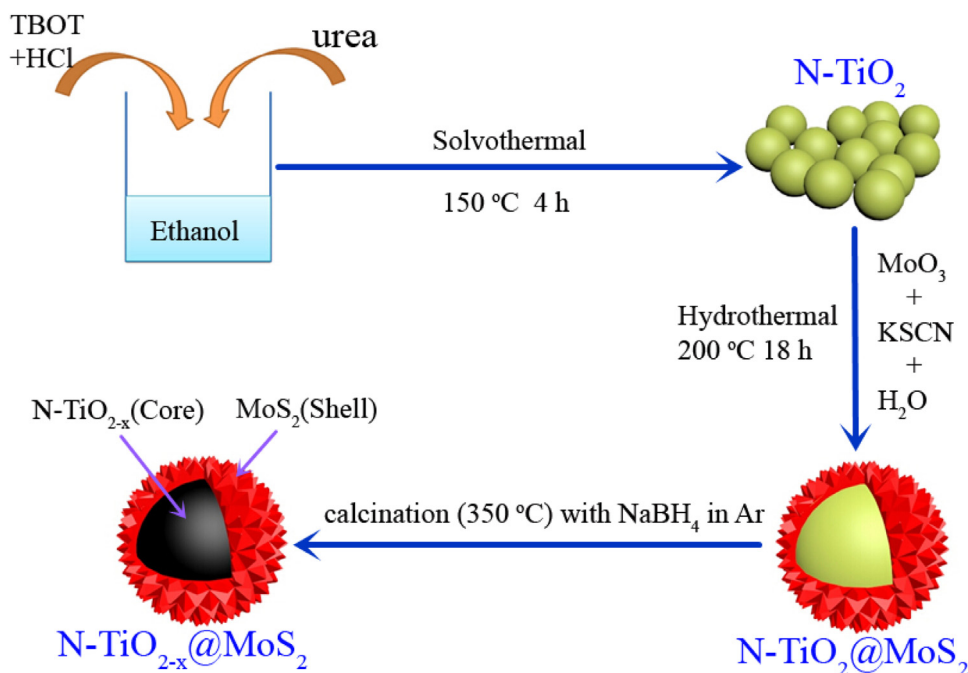
Scheme 1. Schematic diagram for the formation of the N-TiO$_{2-x}$@MoS$_2$ nanocomposites.

ducted in the KOH solution (1 M), which was irradiated by a 300 W Xenon-lamp equipped with a 420 nm cutoff filter.

2.5. Photocatalytic measurement

Photocatalytic hydrogen evolution measurement was carried out in an online photocatalytic hydrogen generation system (AuLight, Beijing, CEL-SPH2N). In a typical photocatalytic hydrogen tests, 50 mg of samples were dispersed in a 100 mL aqueous solution containing the 80 mL of deionized water and 20 mL of methanol used as the sacrificial reagent in closed-gas circulation reaction cell. Before irradiation, the reaction solution was evacuated and purged with N$_2$ several times to completely remove air. An AM 1.5 solar power system (solar simulator (Oriel, USA) equipped with an AM 1.5G filter (Oriel, USA)) was employed as the light irradiation. The hydrogen was periodically analyzed through using an on-line gas chromatography with the interval of each 1 h (SP7800, TCD, molecular sieve 5 Å, N$_2$ carrier, Beijing Keruida, Ltd).

The measurement of photocatalytic activity was carried out at room temperature by the degradation of methyl orange (MO) under visible-light irradiation with a 300 W Xeon-lamp equipped with a 420 nm cut-off filter. In a typical MO degradation test, 50 mg of photocatalyst was added into 50 mL of 10 mg/L MO aqueous solution, which was placed at 20 cm from the light source. Before light irradiation, the suspension was kept in the dark under stirring for 30 min to keep an adsorption-desorption equilibrium. After 120 min photocatalytic reaction, the reaction solution was immediately centrifuged and filtrated. Subsequently, the collected solution was measured at λ = 464 nm by using a T6 UV–vis spectrophotometer for calculating the photocatalytic degradation rate of MO.

3. Results and discussion

The TiO$_2$ is consisted of anatase or rutile crystal phase which may significantly influence the photocatalytic performance and largely determine its suitability in practical applications [37,38]. Therefore, XRD was employed to analyze the crystal phase and crystallinity of these as-prepared samples. As shown in Fig. 1, it is obviously observed that the pure TiO$_2$ and MoS$_2$ are indexed to the
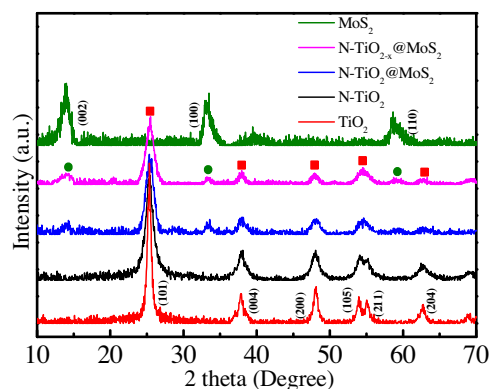

Fig. 1. XRD patterns of TiO$_2$, N-TiO$_2$, N-TiO$_2$@MoS$_2$, N-TiO$_{2-x}$@MoS$_2$ and MoS$_2$, respectively.

anatase phase of TiO$_2$ (JCPDS #21-1272) and the hexagonal phase of MoS$_2$ (JCPDS #37-1492) without any impurity, implying a high purity of the fabricated TiO$_2$ and MoS$_2$ structure. Otherwise, besides the anatase phase of TiO$_2$, no other impurity peak is detected in the N-TiO$_2$. However, the N-TiO$_2$ exhibits a broad anatase (101) peak compared with the pure TiO$_2$, indicating the induction of nitrogen into the TiO$_2$ lattice [39]. For the N-TiO$_2$@MoS$_2$, all of the diffraction peaks can be well indexed to either N-TiO$_2$ or MoS$_2$, which reveals that the hybrid compound is successfully obtained. Moreover, the N-TiO$_{2-x}$@MoS$_2$ still keeps the pristine crystal phase after the process of treatment with NaBH$_4$, but the intensity of N-TiO$_2$ diffraction peaks is evidently decreased and broadened, indicating that its crystalline structure has some variations. According to the related reports, the change of crystalline structure may be ascribed to the production of Ti^{3+} and oxygen vacancy through the chemical reduction treatment [36,40,41]. In addition, for N-TiO$_2$@MoS$_2$ and N-TiO$_{2-x}$@MoS$_2$, the diffraction peak at 14.1° corresponding to the MoS$_2$ (002) plane in the patterns are much weaker than that in the pattern of MoS$_2$, which may ascribe that the intrinsic TiO$_2$ nanostructures prevent the MoS$_2$ nanoflowers from restacking and
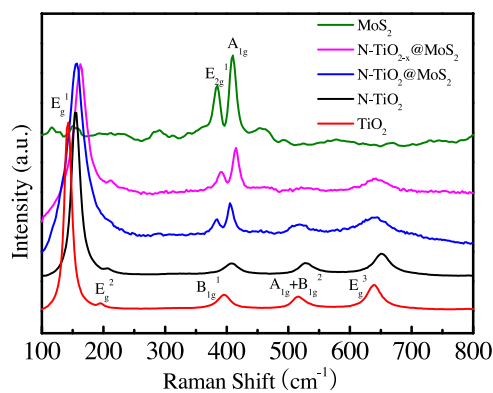
Fig. 2. Raman spectra of TiO_2, $N-TiO_2$, $N-TiO_2@MoS_2$, $N-TiO_{2-x}@MoS_2$ and MoS_2, respectively.

contributes to form the few-layer nanostructure [42]. This result will be demonstrated by TEM, as further discussed below.

To further explore the properties of the hybrid nanostructures among these samples, the Raman spectra of the TiO_2, $N-TiO_2$, $N-TiO_2@MoS_2$, $N-TiO_{2-x}@MoS_2$, and MoS_2 were analyzed in Fig. 2. The characteristic Raman peaks of pure TiO_2 at 143, 196, 394, 516 and 639 cm^{-1} are ascribed to E_g^1, E_g^2, B_{1g}^1, $A_{1g} + B_{1g}^2$ and E_g^3 modes of anatase TiO_2, respectively, and the strongest peak at 143 cm^{-1} is the symmetric stretching modes of O-Ti-O [43]. The two dominant Raman scattering peaks of pure MoS_2 can be observed at 385 and 410 cm^{-1} correspond to E_{2g}^1 and A_{1g} [44]. For $N-TiO_2$, the significant blue shift can be clearly observed and the Raman scattering peaks change slightly weaker compared to the pure TiO_2, indicating that the O or Ti atoms in the lattice of TiO_2 has been replaced by N atom [25,39]. What is more, following to couple with

MoS_2, the E_g^1 peak of $N-TiO_2@MoS_2$ shows a further blue shift. The $A_{1g} + B_{1g}^2$ and E_g^3 oppositely show a red shift compared to the $N-TiO_2$ mostly owing to intimate interactions induced by the wrapped MoS_2 nanoflowers on the $N-TiO_2$ surface [45,46]. Moreover, the B_{1g}^1 peak is replaced by two strong peaks of MoS_2 because of the E_{2g}^1 and A_{1g} vibration modes of MoS_2 [47]. Remarkably, the obvious shift of related peaks for $N-TiO_{2-x}@MoS_2$ demonstrate that the original symmetry of sample lattice is changed after reduction by $NaBH_4$, indicating Ti^{3+} is doped into the lattice [36,41].

The typical scanning electron microscopy (SEM) and transmission electron microscopy (TEM) are used to analyze the morphology and crystal structure of MoS_2 and $N-TiO_{2-x}@MoS_2$. As shown in Fig. 3a, the pure MoS_2 is demonstrated that the hierarchical flowerlike structures which consists of a large number of petals, then we describe it as MoS_2 nanoflower [48]. And the high magnification scanning electron microscopy (SEM) image of pure MoS_2 is shown in Fig. 3b, we can calculate that the thickness of the petals is approximately 2 nm. Furthermore, Fig. 3c and Fig. 3d are the TEM images with different magnifications, which can be clearly seen that each petal is consisted of 4–7 MoS_2 single layer nanosheets with an interlayer spacing of 0.63 nm corresponding to the (002) plane of MoS_2. Fig. S1a presents the morphology of $N-TiO_2$ nanospheres with diameters of 1–2 μm prepared by the solvothermal method. In addition, it can be clearly observed that the $N-TiO_2$ nanospheres are smooth and disperse. Furthermore, Fig. 4a and Fig. 4b obviously reveal that the original $N-TiO_{2-x}$ nanospheres are completely coated by the MoS_2 nanoflowers and a flower-ball structure is displayed, indicating that the 3D $N-TiO_{2-x}@MoS_2$ core-shell structure is successfully formed. In order to demonstrate the effect for morphology during the treatment with $NaBH_4$, the $N-TiO_2@MoS_2$ nanocomposite is shown in Fig. S1b. The morphology of $N-TiO_2@MoS_2$ nanocomposite is also a flower-ball structure, indi-
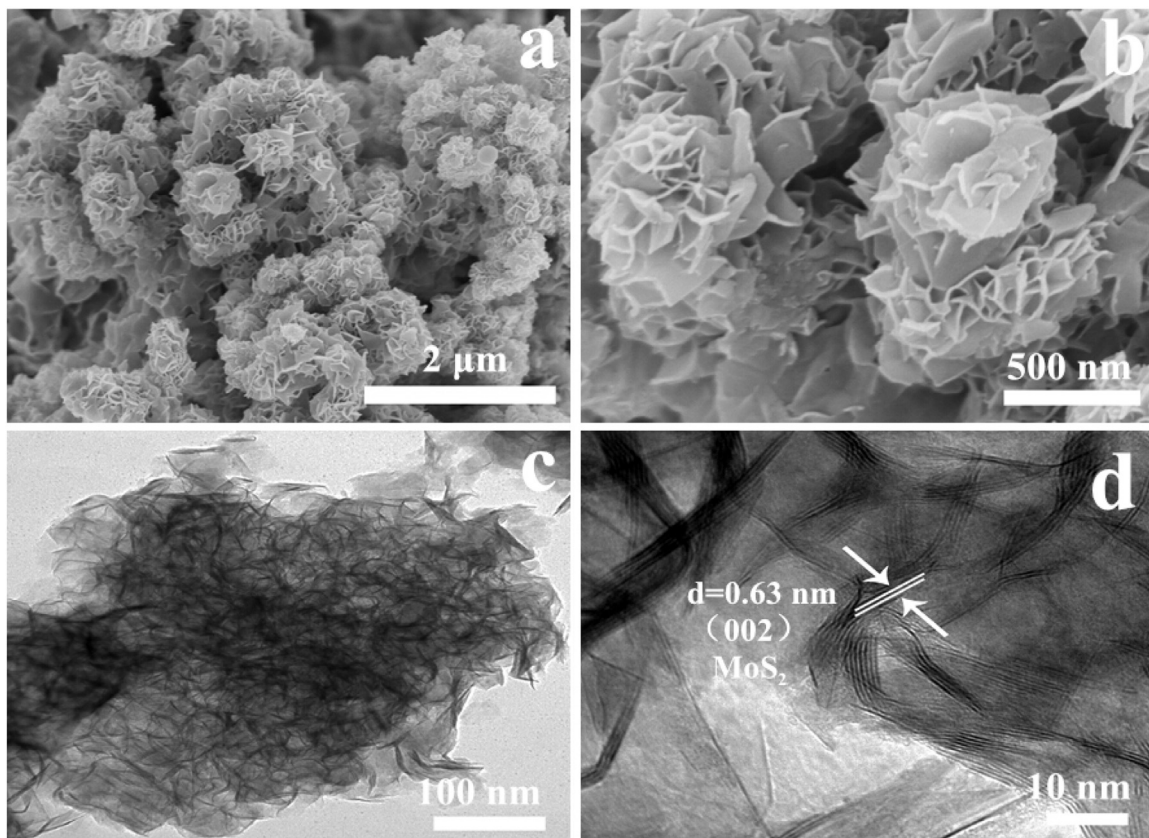

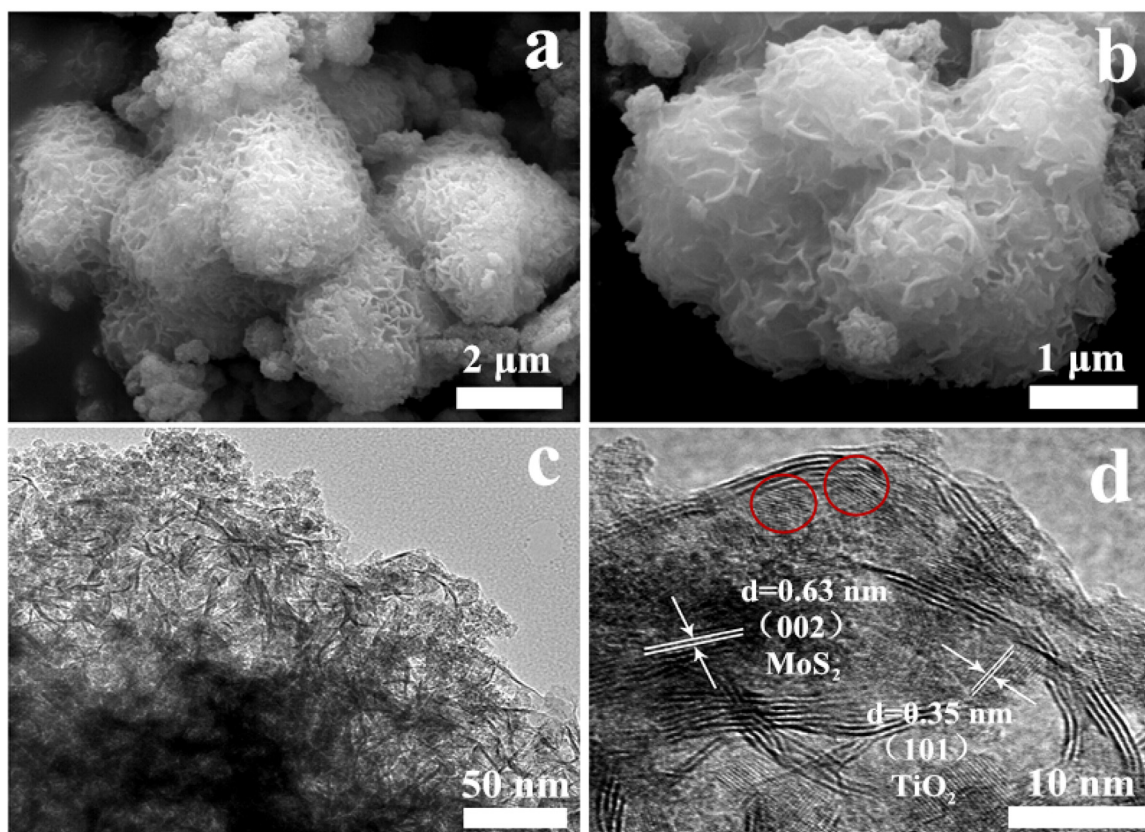**Fig. 3.** SEM (a, b) and TEM images (c, d) of the pure MoS_2 nanoflowers.

Fig. 4. SEM (a, b) and TEM images (c, d) of the N-TiO$_{2-x}$@MoS$_2$ composites.

cating that the in situ solid-state chemical reduction method cannot change the nanostructure of the sample. The TEM images of N-TiO$_{2-x}$@MoS$_2$ composite edges under medium magnification are also displayed in Fig. 4c. It can be easily concluded that the MoS$_2$ nanosheets are also interconnected with each other to forming 3D nanoflowers structure at the edges of N-TiO$_{2-x}$@MoS$_2$ composite. Significantly, the top-view high resolution transmission electron microscopy (HRTEM) image of N-TiO$_{2-x}$@MoS$_2$ shows the few layers MoS$_2$ on the N-TiO$_{2-x}$ nanosphere and the lattice fringe of N-TiO$_{2-x}$ in Fig. 4d and Fig. S2. The 0.63 nm interlayer spacings of the MoS$_2$ nanosheets corresponding to the (002) plane of MoS$_2$ can be obviously seen, revealing a well-defined crystal structure. And the other lattice fringe is approximately 0.35 nm corresponding to the (101) plane of anatase TiO$_2$. Notably, some cross lattice fringes and interlayer spacings which are marked by red circles are found, indicating that heterojunctions are successfully formed between MoS$_2$ and N-TiO$_{2-x}$. Thus the heterojunctions are advantaged to efficiently transfer the photogenerated electrons during the photocatalytic reaction.

In order to investigate surface composition of N-TiO$_{2-x}$@MoS$_2$, the X-ray photoelectron spectroscopy (XPS) was employed to analysis the chemical composition and bonding configuration for the as-prepared sample, and the results are shown in Fig. 5. The full-scale XPS pattern of N-TiO$_{2-x}$@MoS$_2$ is shown in Fig. 5a, which indicates the existence of Ti, O, N, Mo and S elements. What is more, no Na and B elements are detected, revealing that the unreacted NaBH$_4$ can be washed off completely by deionized water. As shown in Fig. 5b, the binding energies of Ti^{4+} 2p$_{1/2}$, Ti^{3+} 2p$_{1/2}$, Ti^{4+} 2p$_{3/2}$ and Ti^{3+} 2p$_{3/2}$ are 463.7, 462.7, 458.0, and 457.0 eV, respectively [49]. The formation of Ti^{3+} species is ascribed to the Ti^{4+} reduction in the process of treatment with NaBH$_4$ [50]. Fig. 5c shows the high-resolution O 1 s XPS spectra, there are three peaks located at 529.2, 529.9 and 531.4 eV, which are attributed to Ti-O bond,oxygen

vacancy (abbr. Ov) neighboring to Ti^{3+} and adsorbed water, respectively [51]. Thus based on the high-resolution Ti 2p and O 1 s spectra, it suggests that Ti^{3+} and Ov are successfully formed. Meanwhile, the high-resolution N 1 s spectra of N-TiO$_{2-x}$@MoS$_2$ are shown in Fig. 5d. We can clearly see that the main peak at binding energy of 399.4 eV is ascribed to the presence of substitutional nitrogen state as the characteristic of O-Ti-N, indicating that partly lattice oxygen was substituted by N atom. On the other hand, a small peak at 400.3 eV can be well assigned to interstitial nitrogen atoms as Ti-O-N in the N-TiO$_{2-x}$@MoS$_2$ [25,52]. As shown in Fig. 5e and Fig. 5f, the binding energies of Mo 3d$_{3/2}$, Mo 3d$_{5/2}$, S 2p$_{1/2}$ and S 2p$_{3/2}$ in the pure MoS$_2$ are located at 232.5, 229.4, 163.4 and 162.2 eV, respectively. However, after coupling with N-TiO$_2$ and the reduction of NaBH$_4$, the Mo 3d$_{3/2}$, Mo 3d$_{5/2}$, S 2p$_{1/2}$ and S 2p$_{3/2}$ peaks shift to 231.2, 228.0, 162.0 and 160.9 eV, respectively, which are lower than the corresponding binding energies of pure MoS$_2$. This result reveals the existence of electronic interactions between MoS$_2$ and N-TiO$_{2-x}$ owing to the electron-attracting capacity of MoS$_2$ and the strong heterostructure effect between the MoS$_2$ nanoflowers and N-TiO$_{2-x}$ nanosphere [53,54]. Therefore, there will be a strong synergistic effect between MoS$_2$ and N-TiO$_{2-x}$ in the 3D N-TiO$_{2-x}$@MoS$_2$ core-shell nanocomposites, which is contributed to significantly enhance the transfer ability of electrons and ions across the interfaces during the hydrogen production process [55,56].

The photocatalytic properties were tested by degrading MO under visible light irradiation, the results are shown in Fig. 6. Considering the possibility that MO can self-degrade by irradiation without catalyst. Therefore, a blank experiment is also carried out as a benchmark. As shown in Fig. 6a and Fig. S3a, the result reveals that no degradation is detected in the 150 min, and thus it can be considered that the self-degradation is negligible. Before
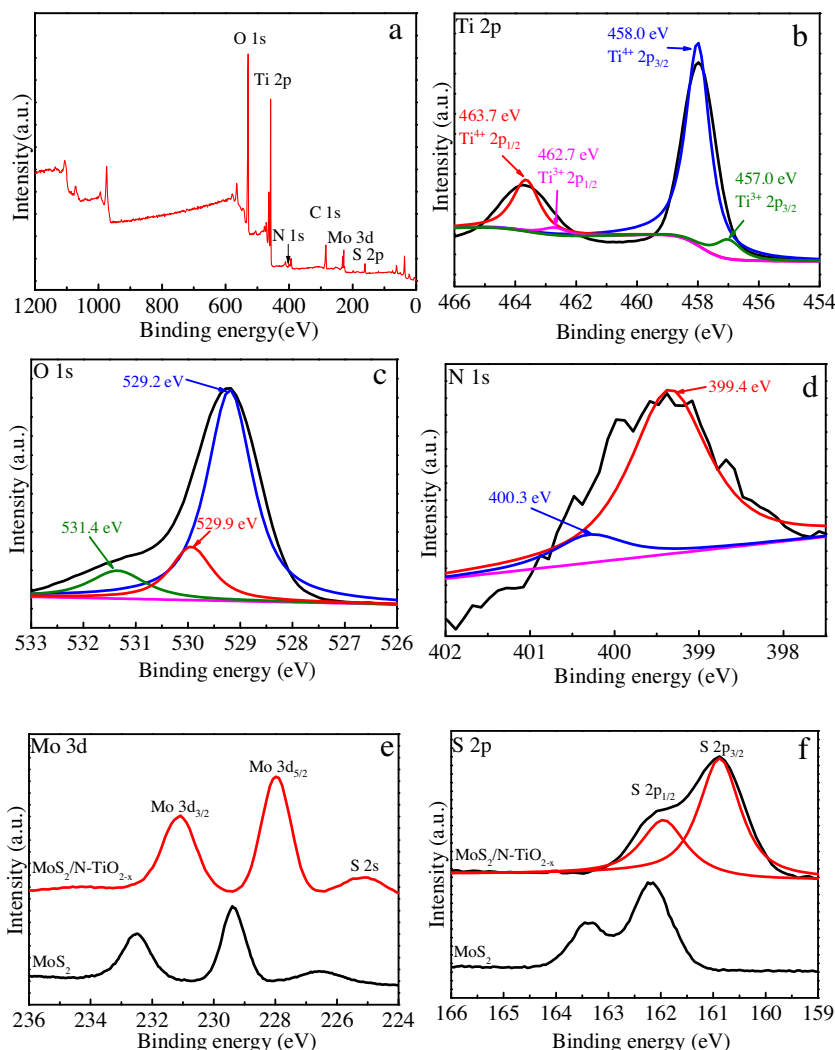
Fig. 5. The full-scale XPS spectra (a), Ti 2p (b), O 1 s (c), N 1 s (d), Mo 3d (e), S 2p (f) for the N-TiO$_{2-x}$@MoS$_2$ and pure MoS$_2$.
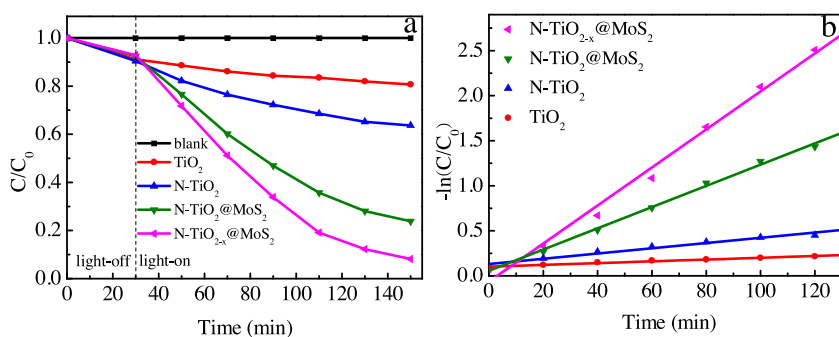

Fig. 6. Photodegradation of MO by using different samples under visible-light irradiation (a), and variations of $-\ln(C/C_0)$ versus visible-light irradiation time with different samples (b) (C is the corresponding degradative concentration of MO and C$_0$ is initial concentration of MO).

irradiation, an adsorption-desorption equilibrium is established. In comparison to pure TiO$_2$, the photocatalytic activity of other samples is all improved under visible light. In particular, the N-TiO$_{2-x}$@MoS$_2$ obviously exhibits the best photodegration ability, which can reach 91.8% of MO removal within 120 min of visible light irradiation. In addition, the first-order rate constants (k) of TiO$_2$, N-TiO$_2$, N-TiO$_2$@MoS$_2$ and N-TiO$_{2-x}$@MoS$_2$ shown in Fig. 6b are 0.0009, 0.0021, 0.0118 and 0.0211 min^{-1}, respectively. Similarly, the N-TiO$_{2-x}$@MoS$_2$ also shows the highest value at 21.3 times

higher than that of pure TiO$_2$, which can be attributed to the synergistic effect between N and Ti^{3+} co-doped and the 3D core-shell structure.

To further demonstrate the wonderful photocatalytic performance of the N-TiO$_{2-x}$@MoS$_2$, the solar-driven hydrogen evolution was also tested through the photocatalytic water splitting process. As shown in Fig. 7a, the hydrogen generation rate of TiO$_2$, N-TiO$_2$ and MoS$_2$ are 0.021, 0.047 and 0.422 mmol h^{-1} g^{-1}, while N-TiO$_2$@MoS$_2$ and N-TiO$_{2-x}$@MoS$_2$ show exceptional hydrogen
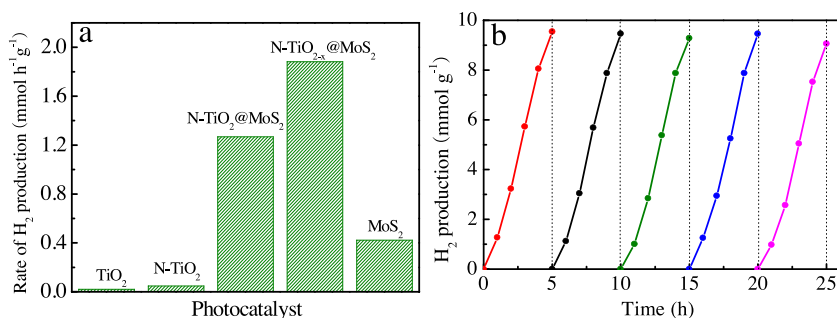
Fig. 7. The photocatalytic H$_2$ evolution (a) of different samples and the recyclability tests (b) of N-TiO$_{2-x}$@MoS$_2$ under AM 1.5.
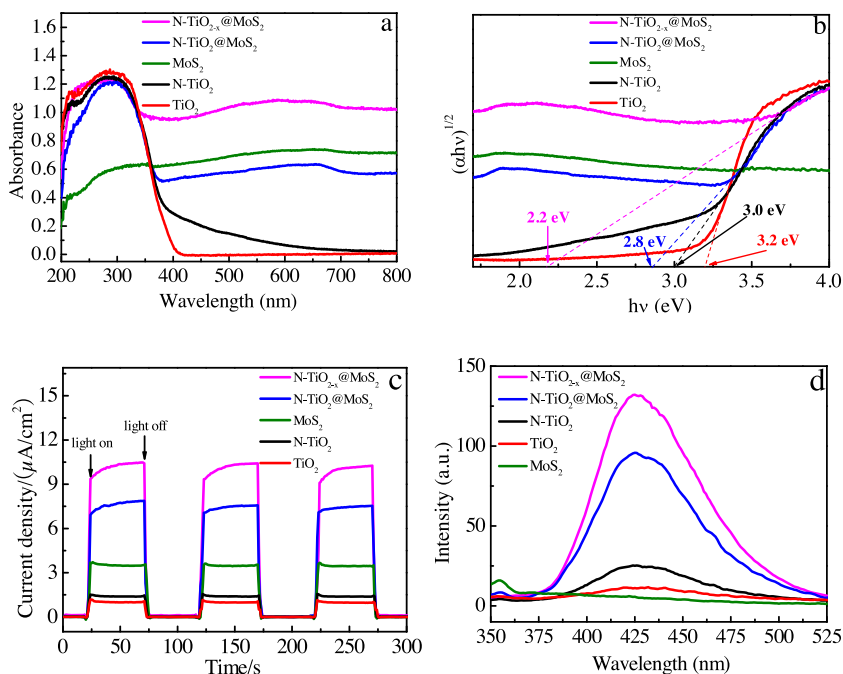

Fig. 8. UV–vis diffuse reflectance spectra (a), determination of the indirect interband transition energies (b), the transient photocurrent responses (c) and fluorescence intensity in 1 h (d) of TiO$_2$, N-TiO$_2$, MoS$_2$, N-TiO$_2$@MoS$_2$ and N-TiO$_{2-x}$@MoS$_2$, respectively.

evolution rates as high as 1.268 and 1.882 mmol h^{-1} g^{-1}. In addition, the hydrogen generation rate of TiO$_{2-x}$@MoS$_2$ is also tested which is shown in Fig. S3b, the hydrogen generation rate is 1.671 mmol h^{-1} g^{-1}. These results indicate that the N-TiO$_{2-x}$@MoS$_2$ has the highest photocatalytic activity among these materials, revealing that the N and Ti^{3+} co-doped and core-shell heterojunction structure contributes to perfect photocatalytic activity. Fig. 7b shows the recycling hydrogen evolution reaction to test the stability of N-TiO$_{2-x}$@MoS$_2$. We can obviously see that N-TiO$_{2-x}$@MoS$_2$ still exhibits nearly constant hydrogen evolution capability after five cycles lasting 25 h in total, indicating the high stability of the photocatalyst.

To explain the photocatalytic properties, the as-prepared samples were analyzed by UV–vis diffuse reflectance spectra, transient photocurrent responses and fluorescence, respectively. As shown in Fig. 8a, the spectra of TiO$_2$ exhibit the typical absorption of semiconductor with a wide band gap, while the MoS$_2$ nanoflowers also show absorption in the UV–vis region. The N-TiO$_2$ has an absorption band edge at about 385 nm. Notably, the visible absorption of the N-TiO$_2$@MoS$_2$ is significantly enhanced after coupling with MoS$_2$. In addition, the N-TiO$_{2-x}$@MoS$_2$ has further absorption in the visible light range compared to the N-TiO$_2$@MoS$_2$ which can be attributed to the introduction of Ti^{3+} and oxygen vacancy [36,41],

resulting in higher light energy utilization. The band gaps of TiO$_2$, N-TiO$_2$, N-TiO$_2$@MoS$_2$ and N-TiO$_{2-x}$@MoS$_2$ are 3.2, 3.0, 2.8 and 2.2 eV, respectively, which are shown in Fig. 8b. What is more, Fig. 8c shows transient photocurrent responses which can be used to analysis the ability of producing charge carriers. The photocurrent of the TiO$_2$, N-TiO$_2$ and MoS$_2$ anode are 1.17, 1.51 and 3.71 μA cm^{-2}, while the photocurrent of the N-TiO$_2$@MoS$_2$ and N-TiO$_{2-x}$@MoS$_2$ anode are 7.85 and 10.42 μA cm^{-2}, which are almost 5 and 7 times higher than that of the N-TiO$_2$. Obviously, the much stronger photocurrent intensity of N-TiO$_2$@MoS$_2$ and N-TiO$_{2-x}$@MoS$_2$ are ascribed to the introduction of MoS$_2$ which contributed to more effectively separated electrons. Therefore, we have no difficulty to conclude that the N and Ti^{3+} co-doping and coupling with MoS$_2$ play significant roles to narrow the band gap and accelerate the charge transfer. Fig. 8d shows the comparative FL intensity of these samples in 1 h under Xenon lamp irradiation with a 420 nm cut-off filter. It is clearly observed that the fluorescence intensity of N-TiO$_{2-x}$@MoS$_2$ is the strongest than any other samples at 425 nm, indicating that the N-TiO$_{2-x}$@MoS$_2$ possess largest amount of ·OH radicals under visible light irradiation, consisting with the photodegradation results of MO.

Based on the above analysis, the possible photocatalytic mechanism of the N-TiO$_{2-x}$@MoS$_2$ sample is proposed as illustrated in
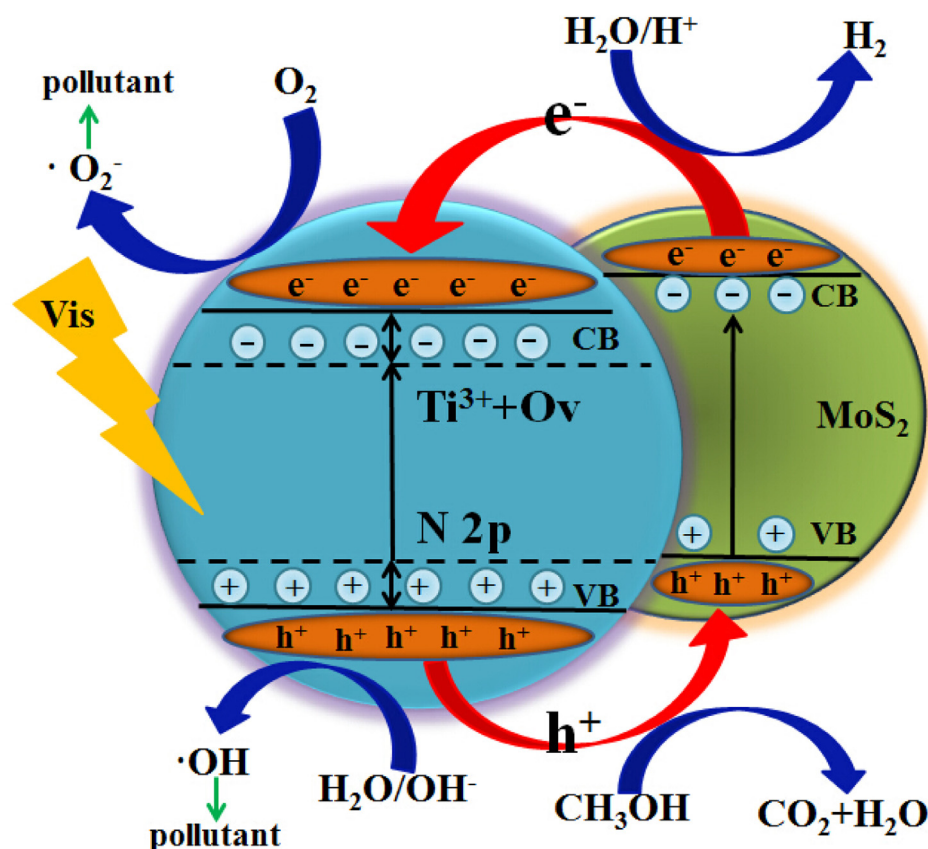
Scheme 2. Schematic illustration of the energy band structure of the N-TiO$_{2-x}$@MoS$_2$ heterostructure and the proposed charge transfer mechanism.

Scheme 2. The doped N species can generate a new impurity level above the valence band (VB) of TiO$_2$ [16,23,25]. Furthermore, the Ti^{3+} and Ov can form a new sublevel state at the bottom of the conduction band (CB) of TiO$_2$ [24,26,41], which combines with a mid-gap state, synergistically narrow the band gap to a lower level and thus enhance the photocatalytic response for the visible light. What is more, after coupling with MoS$_2$ the photocatalytic activity of sample will further be enhanced, because forming core-shell heterojunction structure can not only effectively inhibit the recombination of electron-hole pairs, but also provide abundant catalytic sites for H$_2$ evolution. Therefore, electrons can be consumed to finish a chemical reduction reaction for H$_2$ evolution at these sites [57]. Meanwhile, the holes react with water or hydroxide ions, producing hydroxyl radicals ($^\bullet$OH), and the electrons are trapped on the hybrid surface by absorbing oxygen molecules, producing superoxide anion radicals ($^\bullet$O$_2^-$). Such the $^\bullet$OH and $^\bullet$O$_2^-$ with strong oxidation ability can completely mineralize the organic pollutant. In one word, for our as-prepared photocatalyst, the photogenerated electron-hole pairs are effectively separated and transfer due to the synergistic effects between narrow band gap and heterojunction structure, which are crucial for enhancing photocatalytic activity.

4. Conclusions

In summary, a mild and effective method for synthesizing the 3D N-TiO$_{2-x}$@MoS$_2$ core-shell structured photocatalyst had been designed and developed. The results showed that the obtained photocatalyst was doped with N and Ti^{3+}, and simultaneously coupled with MoS$_2$ to form a N-TiO$_{2-x}$@MoS$_2$ core-shell structure. Significantly, the degradation rate of methyl orange and the hydrogen production rate were as high as 91.8% and 1.882 mmol h^{-1} g^{-1}.

In addition, the wonderful photocatalytic performance of N-TiO$_{2-x}$@MoS$_2$ was attributed to the synergistic effect of N and Ti^{3+} co-doped and introduction of MoS$_2$, which contributed to narrow the band gap and restrain the recombination of electrons-holes. Therefore, the 3D N-TiO$_{2-x}$@MoS$_2$ core-shell structured photocatalyst will be a promising candidate material for wastewater treatment and hydrogen evolution in future.

Appendix A. Supplementary data

Supplementary data associated with this article can be found, in the online version, at http://dx.doi.org/10.1016/j.apcatb.2016.08.031.

References

[1] W. Wang, M.O. Tadé, Z. Shao, Chem. Soc. Rev. 44 (2015) 5371–5408.
[2] L. Zhang, Z. Xing, H. Zhang, Z. Li, X. Wu, X. Zhang, Y. Zhang, W. Zhou, Appl. Catal. B 180 (2016) 521–529.
[3] Z. Xing, W. Zhou, F. Du, Y. Qu, G. Tian, K. Pan, C. Tian, H. Fu, Dalton Trans. 43 (2014) 790–798.

[4] S. Pan, X. Liu, M. Guo, S. Yu, H. Huang, H. Fan, G. Li, J. Mater. Chem. A 3 (2015) 11437–11443.
[5] Y. Duan, J. Zheng, M. Xu, X. Song, N. Fu, Y. Fang, X. Zhou, Y. Lin, F. Pan, J. Mater. Chem. A 3 (2015) 5692–5700.
[6] Z. Liu, Y. Li, C. Liu, J. Ya, L.E.W. Zhao, D. Zhao, L. An, ACS Appl Mater. Interfaces 3 (2011) 1721–1725.
[7] K. Guo, Z. Liu, C. Zhou, J. Han, Y. Zhao, Z. Liu, Y. Li, T. Cui, B. Wang, J. Zhang, Appl. Catal. B 154 (2014) 27–35.
[8] K. Guo, Z. Liu, J. Han, X. Zhang, Y. Li, T. Hong, C. Zhou, J. Power Sources 285 (2015) 185–194.
[9] C. Wang, L. Wu, H. Wang, W. Zuo, Y. Li, J. Liu, Adv. Funct. Mater. 25 (2015) 3524–3533.
[10] G. Moon, W. Kim, A.D. Bokare, N. Sung, W. Choi, Energy Environ. Sci. 7 (2014) 4023–4028.
[11] W. Li, F. Wang, Y. Liu, J. Wang, J. Yang, L. Zhang, A.A. Elzatahry, D. Al-Dahyan, Y. Xia, D. Zhao, Nano Lett. 15 (2015) 2186–2193.
[12] Z. Xing, J. Li, Q. Wang, W. Zhou, G. Tian, K. Pan, C. Tian, J. Zou, H. Fu, Eur. J. Inorg. Chem. 2013 (2013) 2411–2417.
[13] W. Zhou, F. Sun, K. Pan, G. Tian, B. Jiang, Z. Ren, C. Tian, H. Fu, Adv. Funct. Mater. 21 (2011) 1922–1930.
[14] W. Zhou, H. Fu, ChemCatChem 5 (2013) 885–894.
[15] W. Li, M. Liu, S. Feng, X. Li, J. Wang, D. Shen, Y. Li, Z. Sun, A.A. Elzatahry, H. Lu, D. Zhao, Mater. Horiz. 1 (2014) 439–445.
[16] W. Qian, P.A. Greaney, S. Fowler, S. Chiu, A.M. Goforth, J. Jiao, ACS Sustainable Chem. Eng. 2 (2014) 1802–1810.
[17] Z. Xing, Z. Li, X. Wu, G. Wang, W. Zhou, Int. J. Hydrogen Energy 41 (2016) 1535–1541.
[18] Y. Yuan, Z. Ye, H. Lu, B. Hu, Y. Li, D. Chen, J. Zhong, Z. Yu, Z. Zou, ACS Catal. 6 (2016) 532–541.
[19] W. Li, D. Zhao, Adv. Mater. 25 (2013) 5129–5152.
[20] H. Liu, W. Li, D. Shen, D. Zhao, G. Wang, J. Am. Chem. Soc. 137 (2015) 13161–13166.
[21] S. Pany, K.M. Parida, Phys. Chem. Chem. Phys. 17 (2015) 8070–8077.
[22] Y. Yu, Y. Tang, J. Yuan, Q. Wu, W. Zheng, Y. Cao, J. Phys. Chem. C 118 (2014) 13545–13551.
[23] R. Asahi, T. Morikawa, T. Ohwaki, K. Aoki, Y. Taga, Science 293 (2001) 269–271.
[24] X. Chen, L. Liu, P. Yu, S. Mao, Science 331 (2011) 746–750.
[25] D. Li, J. Jia, T. Zheng, X. Cheng, X. Yu, Appl. Catal. B: Environ. 188 (2016) 259–271.
[26] X. Chen, L. Liu, F. Huang, Chem. Soc. Rev. 44 (2015) 1861–1885.
[27] S. Hoang, S.P. Berglund, N.T. Hahn, A.J. Bard, C.B. Mullins, J. Am. Chem. Soc. 134 (2012) 3659–3662.
[28] S. Tan, A. Ambrosi, Z. Sofer, Š. Huber, D. Sedmidubský, M. Pumera, Chem.-Eur. J. 21 (2015) 7170–7178.
[29] L. Hu, Y. Ren, H. Yang, Q. Xu, ACS Appl. Mater. Interfaces 6 (2014) 14644–14652.
[30] X. Yu, H. Hu, Y. Wang, H. Chen, X.W. (David) Lou, Angew. Chem. 127 (2015) 7503–7506.
[31] G. Ye, Y. Gong, J. Lin, B. Li, Y. He, S.T. Pantelides, W. Zhou, R. Vajtai, P.M. Ajayan, Nano Lett. 16 (2016) 1097–1103.
[32] M. Yang, C. Han, Y. Xu, J. Phys. Chem. C 119 (2015) 27234–27246.
[33] T. Lin, B. Kang, M. Jeon, C. Huffman, J. Jeon, S. Lee, W. Han, Ji. Lee, S. Lee, G. Yeom, K. Kim, ACS Appl. Mater. Interfaces 7 (2015) 15892–15897.
[34] Q. Xiang, J. Yu, M. Jaroniec, J. Am. Chem. Soc. 134 (2012) 6575–6578.
[35] C. Meng, Z. Liu, T. Zhang, J. Zhai, Green Chem. 17 (2015) 2764–2768.
[36] H. Tan, Z. Zhao, M. Niu, C. Mao, D. Cao, D. Cheng, P. Feng, Z. Sun, Nanoscale 6 (2014) 10216–10223.
[37] Z. Xing, W. Zhou, F. Du, L. Zhang, Z. Li, H. Zhang, W. Li, ACS Appl. Mater. Interfaces 6 (2014) 16653–16660.
[38] Z. Xing, H. Zhang, Z. Li, X. Zhang, Y. Zhang, L. Li, W. Zhou, ChemPlusChem 80 (2015) 623–629.
[39] A.P. Bhirud, S.D. Sathaye, R.P. Waichal, J.D. Ambekar, C. Park, B.B. Kale, Nanoscale 7 (2015) 5023–5034.
[40] J. Huo, Y. Hu, H. Jiang, C. Li, Nanoscale 6 (2014) 9078–9084.
[41] W. Zhou, W. Li, J. Wang, Y. Qu, Y. Yang, Y. Xie, K. Zhang, L. Wang, H. Fu, D. Zhao, J. Am. Chem. Soc. 136 (2014) 9280–9283.
[42] B. Guo, K. Yu, H. Fu, Q. Hua, R. Qi, H. Li, H. Song, S. Guo, Z. Zhu, J. Mater. Chem. A 3 (2015) 6392–6401.
[43] H. Li, Y. Wang, G. Chen, Y. Sang, H. Jiang, J. He, X. Li, H. Liu, Nanoscale 8 (2016) 6101–6109.
[44] M. Shen, Z. Yan, L. Yang, P. Du, J. Zhang, B. Xiang, Chem. Commun. 50 (2014) 15447–15449.
[45] W. Zhou, Z. Yin, Y. Du, X. Huang, Z. Zeng, Z. Fan, H. Liu, J. Wang, H. Zhang, Small 9 (2013) 140–147.
[46] Y. Zhu, Q. Ling, Y. Liu, H. Wang, Y. Zhu, Phys. Chem. Chem. Phys. 17 (2015) 933–940.
[47] Q. Xiang, J. Yu, M. Jaroniec, J. Am. Chem. Soc. 134 (2012) 6575–6578.
[48] H. Fu, K. Yu, H. Li, J. Li, B. Guo, Y. Tan, C. Song, Z. Zhu, Dalton Trans. 44 (2015) 1664–1672.
[49] G. Li, J. Li, G. Li, G. Jiang, J. Mater. Chem. A 3 (2015) 22073–22080.
[50] W. Fang, M. Xing, J. Zhang, Appl. Catal. B 160 (2014) 240–246.
[51] W. Hu, W. Zhou, K. Zhang, X. Zhang, L. Wang, B. Jiang, G. Tian, D. Zhao, H. Fu, J. Mater. Chem. A 4 (2016) 7495–7502.
[52] X. Yu, L. Wang, J. Zhang, W. Guo, Q. Zhao, Y. Qin, X. Mou, A. Li, H. Liu, J. Mater. Chem. A 3 (2015) 19129–19136.
[53] B. Chen, N. Zhao, L. Guo, F. He, C. Shi, C. He, J. Li, E. Liu, Nanoscale 7 (2015) 12895–12905.
[54] C. Li, L. Wang, Y. Tang, S. Luo, Y. Liu, S. Zhang, Y. Zeng, Y. Xu, Appl. Catal. B 164 (2015) 1–9.
[55] W. Li, J. Yang, Z. Wu, J. Wang, B. Li, S. Feng, Y. Deng, F. Zhang, D. Zhao, J. Am. Chem. Soc. 134 (2012) 11864–11867.
[56] X. Liu, Z. Xing, H. Zhang, W. Wang, Y. Zhang, Z. Li, X. Wu, X. Yu, W. Zhou, ChemSusChem 9 (2016) 1118–1124.
[57] Y. Yuan, D. Chen, Y. Huang, Z. Yu, J. Zhong, T. Chen, W. Tu, Z. Guan, D. Cao, Z. Zou, ChemSusChem 9 (2016) 1003–1009.